THE SOLIDIFICATION VELOCITY OF UNDERCOOLED NICKEL AND TITANIUM ALLOYS WITH DILUTE SOLUTE

P.R. Algoso[1], A.S. Altgilbers[2], W.H. Hofmeister[1] and R.J. Bayuzick[1]*

[1]Vanderbilt University, [2]Federal-Mogul Corporation

Introduction

The study of solidification velocity is important for two reasons. First, understanding the manner in which the degree of undercooling of the liquid and solidification velocity affect the microstructure of the solid is fundamental. Second, there is disagreement between theoretical predictions of the relationship between undercooling and solidification velocity and experimental results.

Thus, the objective of this research is to accurately and systematically quantify the solidification velocity as a function of undercooling for dilute nickel- and titanium-based alloys. The alloys chosen for study cover a wide range of equilibrium partition coefficients, and the results are compared to current theory.

The IMS Model

Boettinger, Coriell, and Trivedi[1] formulated one of the most widely used models for describing the nature of the solidification velocity of undercooled metal systems. The model combines the Ivantsov[2] solution for the diffusional fields about a paraboloid of revolution with the marginal stability arguments of Langer and Müller-Krumbhaar[3] and non-equilibrium interface conditions as determined by Aziz and Kaplan[4,5]. Together, they form what is referred to as the BCT theory or IMS model for rapid solidification. The model predicts solidification velocity as a function of undercooling for dilute alloys.

Boettinger et al[1] give the total undercooling, ΔT, as

$$\Delta T = \left(\frac{L}{C}\right) Iv(P_t) + m_L C_o \left[1 - \frac{m_L'/m_L}{1-(1-k)Iv(P_c)} \right] + \frac{2T_m \Gamma}{r} + \frac{RT_m^2}{L}\frac{V}{V_o} \qquad (1)$$

where L is the latent heat of fusion, C is the heat capacity, Iv(x) is the Ivantsov function, m_L is the liquidus slope, C_o is the alloy concentration, T_m is the melting temperature, Γ is the Gibbs-Thomson coefficient (ratio of interfacial energy, σ, to the entropy of fusion), r is the dendrite tip radius, R is the gas constant, V is the dendrite tip velocity, and V_o is the speed of sound in the liquid. The thermal and solutal Peclet numbers, P_t and P_c respectively, are given as

$$P_t = \frac{Vr}{2\alpha} \qquad (2)$$

and

$$P_c = \frac{Vr}{2D} \qquad (3)$$

where α is the thermal diffusivity and D is the solutal diffusivity. The partition coefficient, k, is given as

* Corresponding author. email: robert.j.bayuzick@vanderbilt.edu

$$k = \frac{k_E + \beta_0 V}{1 + \beta_0 V} \qquad (4)$$

where k_E is the equilibrium partition coefficient. The solute trapping kinetic parameter, β_0, is given as

$$\beta_0 = \frac{a_0}{D} \qquad (5)$$

where a_0 is the diffusive length scale. The effective liquidus slope, m_L' is given as

$$m_L' = m_L \left[1 + \frac{k_E - k\left(1 - \ln\frac{k}{k_E}\right)}{1 - k_E} \right] \qquad (6)$$

The marginal stability criterion is used to decouple V and r, since they are not uniquely specified by the equation 1. The dendrite tip radius, r, is given as

$$r = \frac{T_m \Gamma / \sigma^*}{\left(\frac{L}{C}\right) P_t \xi_t + \frac{2 m_L C_o (k-1)}{1 - (1-k) Iv(P_c)} \xi_c} \qquad (7)$$

where

$$\xi_t = 1 - \frac{1}{\sqrt{1 + \left(\sigma^* P_t^2\right)^{-1}}} \qquad (8)$$

and

$$\xi_c = 1 + \frac{2k}{1 - 2k - \sqrt{1 + \left(\sigma^* P_c^2\right)^{-1}}} \qquad (9)$$

The marginal stability parameter, σ^*, is often taken to be[1] a constant equal to $(4\pi^2)^{-1}$.

The IMS model predicts an increase in solidification velocity with increasing undercooling at low undercoolings. In this low undercooling regime, dendrite growth is solutally controlled. Eventually, the curve reaches a plateau, and then rapidly increases during a transition to thermally controlled growth accompanied by solute trapping.

The prediction of the solidification velocity by the IMS model depends on the selection of thermophysical properties used in the calculations. Of the thermophysical properties in the model, the following parameters are reasonably well known for a given alloy: T_m, L, C, m_L, C_o, k_E, and V_o. The remaining parameters are equivocal and are known within an order of magnitude: D, a_0, α, and σ. In general for most metals, D is on the order of 10^{-9} to $10^{-8} m^2/s$, a_0 is on the order of 10^{-10} to $10^{-9} m$, α is on the order of 10^{-6} to $10^{-5} m^2/s$, and σ is roughly 0.15 to $0.35 J/m^2$. Because of the uncertainty associated with these equivocal parameters, these variables can be "adjustable" in the model to determine if IMS modeling will fit experimental results.

In order to test the sensitivity of the IMS model to variations in the equivocal parameters, calculations were made by adjusting one equivocal variable of interest while holding all others constant. The parameters used for the sensitivity analyses are shown in table 1, and the results are shown in figure 1. Due to the small

64

numerical range of interfacial energy and its limited effect on the overall shape of the solidification velocity versus undercooling curve, the effect of varying σ is not a main consideration for sensitivity analysis.

Using a dilute nickel-based alloy ($1^a/_o$ solute), the effect of varying β_o is shown in figure 1a. This shows that the velocity at which the plateau appears increases with decreasing β_o. This is expected since faster diffusing species (or shorter diffusional length scales) would cause the solidification velocity plateau to appear at higher velocities. In figure 1a, β_o was varied by holding D constant while varying a_o. An equivalent analysis may be conducted by holding a_o constant while varying D. This would result in curves that although may be numerically different than figure 1, would exhibit the same relationship between plateau velocity and β_o.

The effect of varying α is shown in figure 1b. The solidification velocity is decreased at higher undercoolings with decreasing thermal diffusivity. Since the higher undercooling regime involves thermally controlled growth, lower thermal diffusivities will cause slower solidification velocities. Lower thermal diffusivities also damp the appearance of a velocity plateau, as the transition from solutally controlled growth to thermally controlled growth becomes indistinguishable with respect to its velocity. Thus, figure 1b also demonstrates that certain values for the IMS model parameters could describe a set of conditions such that a transition in growth behavior would not manifest itself in plateaus or other abrupt changes in the solidification velocity versus undercooling curve. Another possibility is that solidification velocity is entirely dominated by one growth behavior or another for certain values of IMS model parameters. In these cases, the curve would appear to be smooth and closely approximate a parabolic or power law.

The solute species in an alloy determines k_E and m_L for the IMS model calculation; these variables are reasonably well known for a given alloy system. The sensitivity analysis in figure 1c shows how the solidification velocity versus undercooling curve changes as a function of solute species. Figure 1c shows the effect of varying k_E and illustrates that the plateau in solidification velocity is damped for large values of k_E. Because large k_E alloys are predicted to exhibit weak partitioning across the solid-liquid interface during solidification, the IMS model does not contain a noticeable plateau in the solidification velocity versus undercooling curve. Thus, the IMS model predicts that the solidification velocity plateau should only appear for small k_E alloys. For most metals, m_L has a range of approximately -2 to -30K/at%. While the value of m_L has large quantitative effects on the IMS model, the shape of the solidification velocity versus undercooling curve is not greatly affected. As predicted by the IMS model, small k_E alloys have a pronounced solidification velocity plateau, while large k_E alloys do not regardless of the value of m_L.

Table 1: IMS model parameters used in numerical sensitivity analysis for a dilute nickel-based alloy in figure 1.

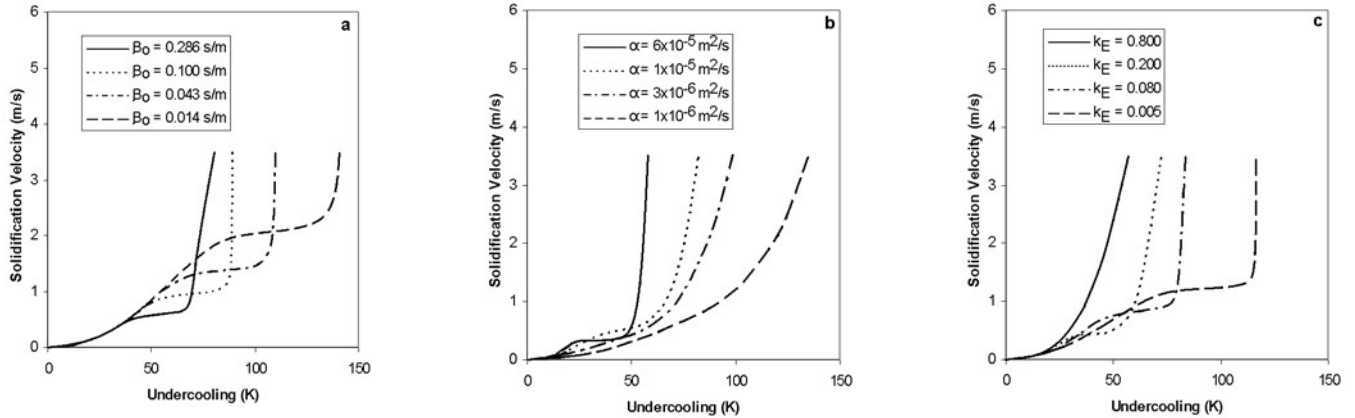|	Effect of varying solute trapping kinetic parameter in figure 1a	Effect of varying thermal diffusivity in figure 1b	Effect of varying equilibrium partition coefficient in figure 1c
T_m (K)	1726	1726	1726
L (J/mol)	17120	17120	17120
C (J/molK)	43	43	43
k_E	0.005	0.2	Variable
a_o (m)	Variable	2×10^{-10}	7×10^{-10}
m_L (K/at%)	-10.6	-10.6	-10.6
C_o (at%)	1	1	1
α (m²/s)	10^{-5}	Variable	10^{-5}
D (m²/s)	7×10^{-9}	7×10^{-9}	7×10^{-9}
V_o (m/s)	4036	4036	4036
σ (J/m²)	0.23	0.23	0.23

Figure 1: Sensitivity analysis of IMS model with one parameter varied while all others held constant. Variable parameters: (a) solute trapping kinetic parameter, β_o, with D held constant and a_o varied, (b) thermal diffusivity, α, and (c) equilibrium partition coefficient, k_E.

The Effect of Oxygen in Pure Metals

There is disagreement between theory and experimental results as well as wide data scatter between various experimenters in ground-based research efforts. The solidification velocity of pure nickel was measured by several experimenters[6-13], and the results are shown in figure 2. This composite plot shows that at undercoolings less than 10% of the melting temperature, T_m, solidification velocity is observed as increasing for increasing undercooling. At undercoolings greater than $10\%T_m$, there is wide divergence in solidification velocity results. At the upper limit of solidification velocity, Walker et al[6] show a continuously increasing velocity with increasing undercooling, while the results of Bassler et al[9] show a velocity plateau at high undercoolings.
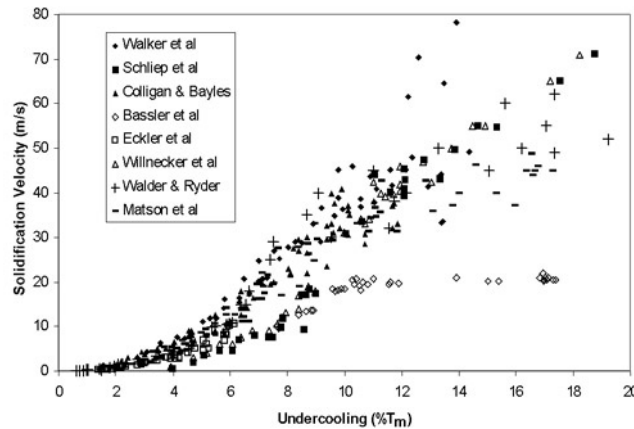

Figure 2: Solidification velocity of pure nickel as measured by several experimenters[6-13].

Bassler[14] and Walder and Ryder[12] measured the solidification velocity of pure titanium as a function of undercooling, and the results are shown in figure 3. Both studies show a continuous rise in solidification velocity with increasing undercooling.

Bassler[14] measured the solidification velocity of pure nickel in three different processing environments: He-H$_2$, UHP He, and with an air leak in the system. The results are shown in figure 4. The different

66

environments were used to determine the effect of oxygen on the solidification of pure nickel. He-H$_2$ was used as an oxygen-reducing environment, while the UHP He and air leak environments increased the oxygen content in the system during processing. The results show that for low oxygen environments, the solidification velocity of pure nickel increases with increasing undercooling until reaching a velocity plateau at high undercooling. Solidification velocities as a function of undercooling were lower for samples processed in the UHP He environment, but velocity also increases until reaching a plateau at high undercooling. Finally, for those samples processed with an air leak in the system, solidification velocity was markedly suppressed for the entire range of undercoolings.

Cochrane et al[15] measured the solidification velocity of pure copper for one set of samples containing approximately 10ppm oxygen and another set of samples containing an average concentration of approximately 600ppm oxygen. The results are shown in figure 5 along with the theoretical prediction of Lipton, Kurz and Trivedi[16] (LKT theory). For the samples with a higher oxygen concentration, solidification velocities are lower than those for the low oxygen concentration samples. Additionally, these higher oxygen concentration samples deviate from theory above 200K undercooling.

Obviously, figures 2 through 5 illustrate the effects of oxygen on the solidification velocity of pure metals. In "pure" nickel and "pure" copper, residual oxygen reduces solidification velocities at all undercoolings and depending on concentration, produces a plateau in solidification velocity at high undercoolings. In "pure" titanium, no plateau in solidification velocity is reached at high undercoolings.

Experimental Method
Solidification velocity measurements of undercooled melts are accomplished in Vanderbilt's electromagnetic levitator. Containerless processing by electromagnetic levitation allows for large degrees of undercooling to be readily achieved, and allows for direct observation of the sample surface during recalescence. Thermal imaging techniques are used to capture the recalescence event, while optical pyrometry is used to measure bulk temperature. A schematic diagram of Vanderbilt's electromagnetic levitator is shown in figure 6.

Two means of thermal imaging are utilized in solidification velocity measurements. For low undercoolings (<5%T$_m$), a Dalsa digital CCD camera is used. The Dalsa camera is an 8-bit camera with 64x64 pixel resolution and is able to capture 1,400 frames per second. This camera is useful for recording solidification velocities less than 4 m/s. For intermediate and high undercoolings, a high-speed data acquisition system[17] (HSDA96) is used. The HSDA96 is an 8-bit system featuring a 10x10 array of parallel-tapped photodiodes capable of capturing thermal images at 1 million frames per second. The experimental error associated with determining solidification velocity using thermal imaging techniques is ±10%[14]. Thermal images captured using the Dalsa camera and HSDA96 are shown in figure 7.

While a large number of experiments on numerous alloys have been conducted at Vanderbilt, only the results of the following alloys are reported here: Ni-C, k$_E$=0.1-0.2; Ti-Ni, k$_E$=0.2-0.3; Ni-Sn, k$_E$=0.3-0.5; Ni-Cu, k$_E$=0.6-0.7; and Ni-Ti, k$_E$=0.8-0.9. These alloys were selected to represent a wide range of equilibrium partition coefficients.

Experimental Results

The solidification velocity measurements as a function of undercooling for the alloys are shown in figures 8 through 12. All alloys exhibit two plateaus with the exception of Ti-1^a/$_o$Ni in figure 9a (which only exhibits one plateau). The first plateau occurs at intermediate undercoolings, while the second plateau occurs at high undercoolings. It should be noted that no plateau at intermediate undercoolings appears in the results for the pure elements (figures 2-5) and, therefore, this intermediate plateau is a direct result of solute addition.

Altgilbers[18] analyzed the microstructures of the processed samples as a function of undercooling and concluded that the first plateau is accompanied by a change in solidification morphology. Solidification morphology is dendritic for undercoolings less than that of the first plateau, while at higher undercoolings the morphology is cellular. In the second plateau, there is no distinguishable change in morphology and the structure remains cellular. The surface micrographs of Ni-10^a/$_o$Ti are shown in figure 13 as an example.

Altgilbers[18] also conducted a microprobe analysis on Ni-10^a/$_o$Ti; the results are shown in figure 14. Figure 14 shows the nature of the decrease in the concentration difference across the dendrite tips as undercooling increases. The large decrease in concentration difference occurs at intermediate undercoolings in the range of the first plateau in Ni-10^a/$_o$Ti and is therefore indicative of the onset of solute trapping.
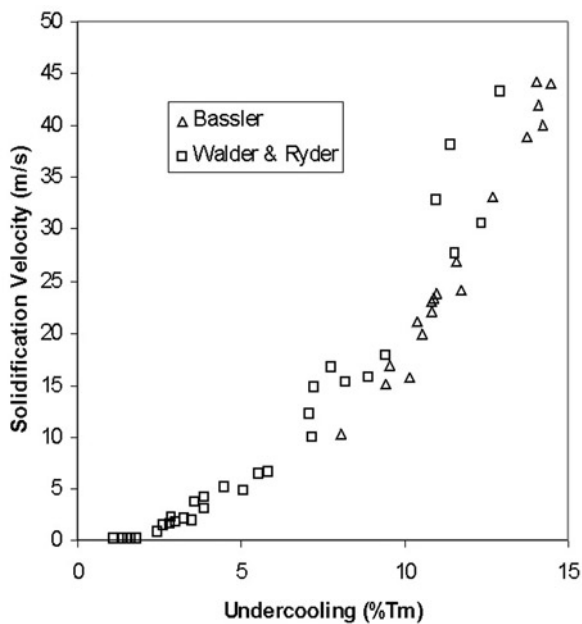
Figure 3: Solidification velocity of pure titanium as measured by Bassler[14] and Walder and Ryder[12].
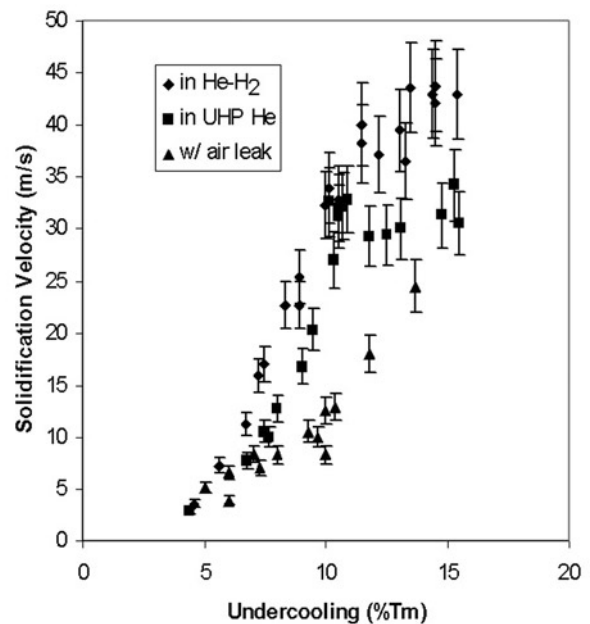
Figure 4: Solidification velocity of pure nickel in three different processing environments as measured by Bassler[14].
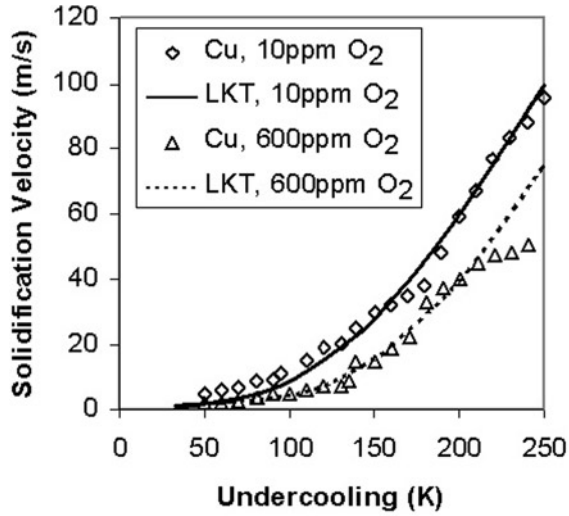
Figure 5: Solidification velocity of pure copper with two different oxygen concentrations by Cochrane et al[15].
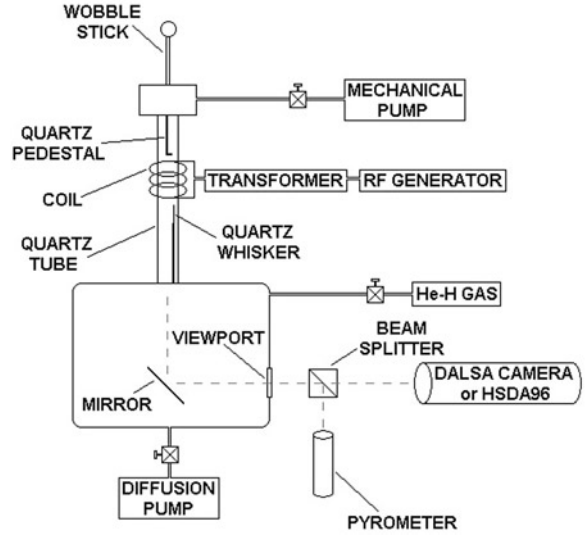

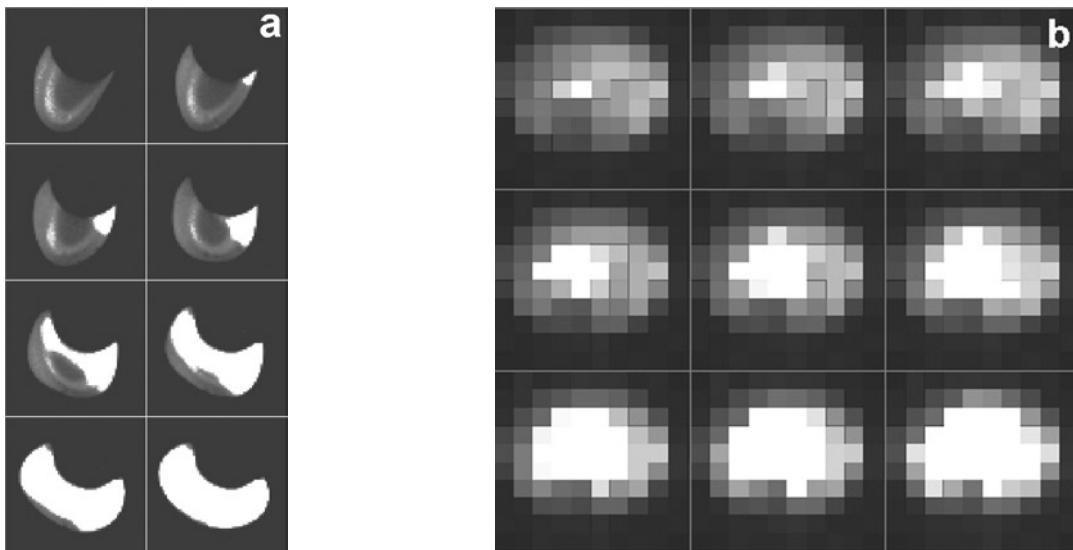Figure 6: Schematic diagram of Vanderbilt's electromagnetic levitator.

Figure 7: Thermal images of solidification taken with (a) Dalsa camera, Ni-based sample, 1.4ms per frame, solidification velocity = 0.6m/s and (b) HSDA96, Ti-based sample, 40μs per frame, solidification velocity = 16m/s. Bright areas represent solid, and dark areas represent undercooled liquid.
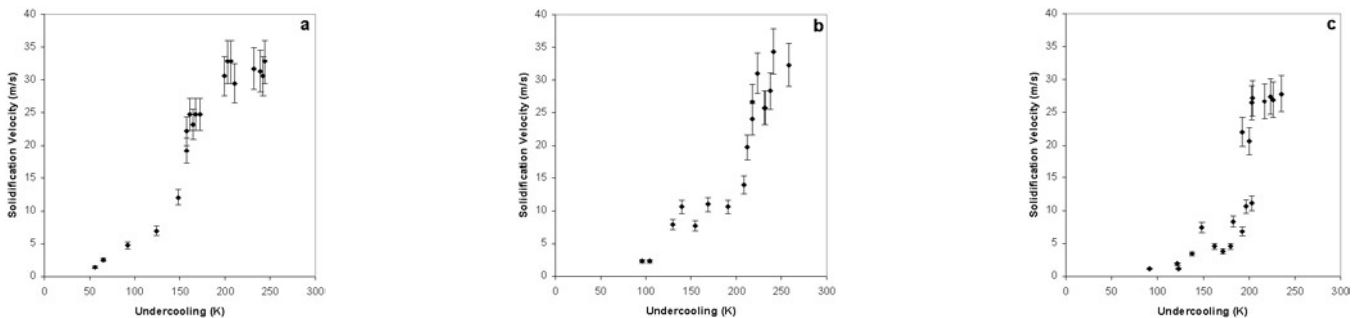

Figure 8: Solidification velocity of (a) Ni-0.6$^a/_o$C, (b) Ni-1.7$^a/_o$C and (c) Ni-2.8$^a/_o$C.
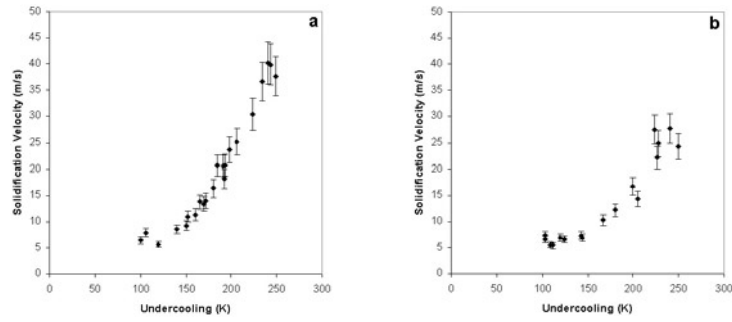
Figure 9: Solidification velocity of (a) Ti-1^a/$_o$Ni and (b) Ti-2^a/$_o$Ni.
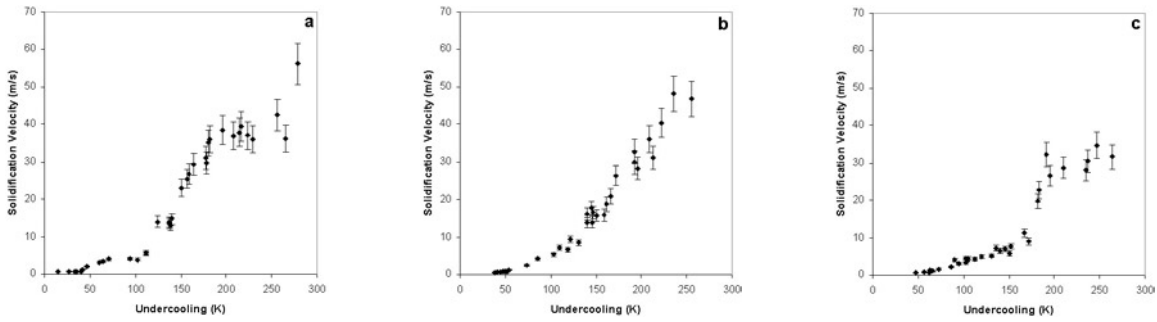
Figure 10: Solidification velocity of (a) Ni-1^a/$_o$Sn, (b) Ni-2.5^a/$_o$Sn and (c) Ni-4^a/$_o$Sn.
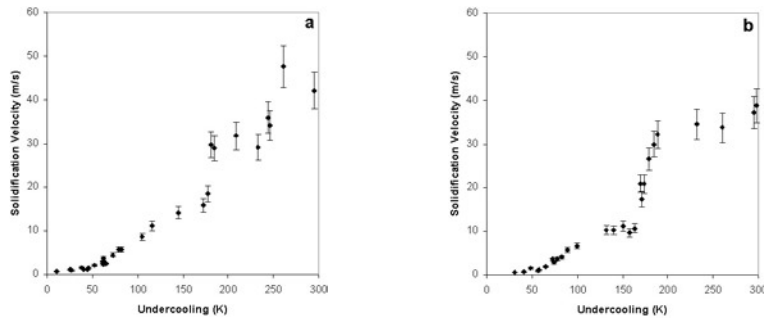

Figure 11: Solidification velocity of (a) Ni-5^a/$_o$Cu and (b) Ni-10^a/$_o$Cu.
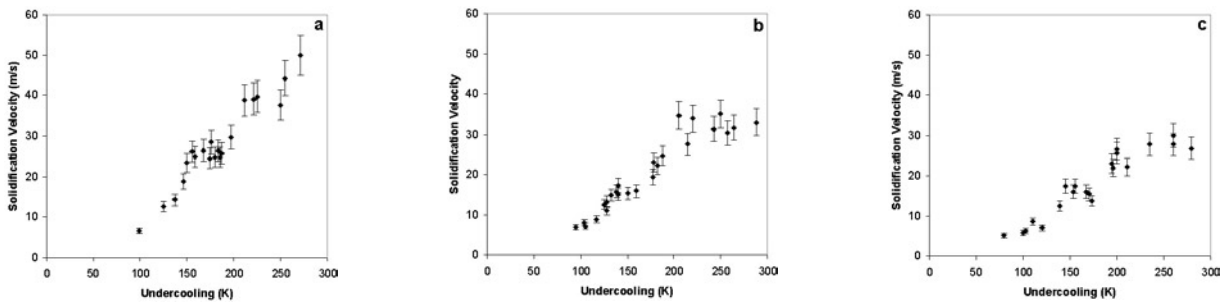
Figure 12: Solidification velocity of (a) Ni-3^a/$_o$Ti, (b) Ni-5^a/$_o$Ti and (c) Ni-10^a/$_o$Ti.
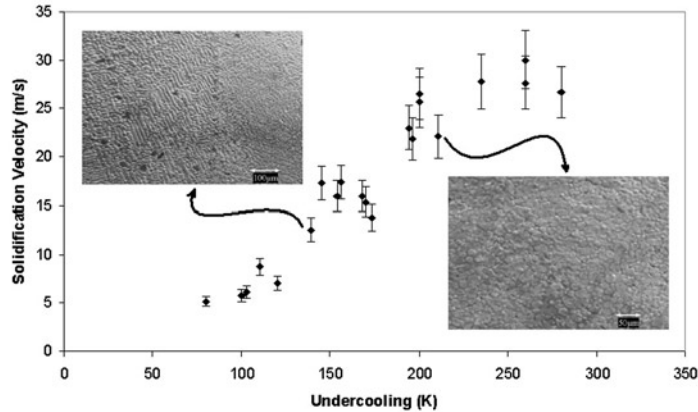
70

Figure 13: Microstructures of Ni-10$^a/_o$Ti samples. At velocities below the first plateau, the solidification morphology is dendritic, while at higher velocities the morphology is cellular.
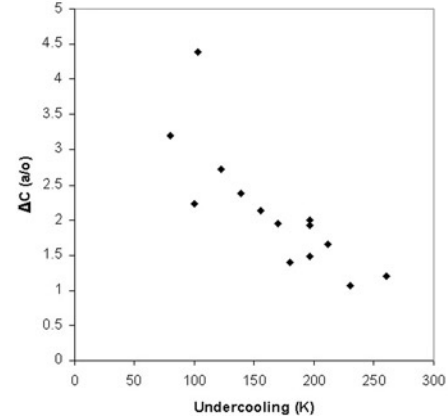

Figure 14: Microprobe analysis of Ni-10$^a/_o$Ti samples showing a decrease in concentration difference across the dendrite tips with increasing undercooling.

Based on the results of residual oxygen's effects on the solidification velocity of pure elements at high undercoolings, it is hypothesized that the second plateau in the results for the alloys is also due to residual oxygen in the alloy system. Further investigation of solidification velocity while varying oxygen concentrations in alloys is required since interaction between solutes and oxygen may play a role in solidification behavior.

Application of IMS Modeling
The IMS model was applied to the results to test the agreement between theory and experiment. As examples, one of each of the results of the smallest k_E alloy (Ni-C) and largest k_E alloy (Ni-Ti) are plotted along with the IMS model in figures 15 and 16 respectively. Figures 15 and 16 show similar results. For both low k_E and high k_E examples, good agreement can only be attained by using a k_E in the calculations that is much smaller than the actual k_E. The parameters used for calculation of the solidification velocity versus undercooling curve for figures 15 and 16 are shown in table 2.

Conclusions
Solidification velocity decreases with increasing amounts of residual oxygen in otherwise pure nickel for all ranges of undercooling. Depending on the oxygen concentration, a solidification velocity plateau may appear in higher undercoolings.

In most alloys, there are two plateaus in the solidification velocity versus undercooling plot. The first plateau occurs in intermediate undercoolings and is a direct result of solute addition. Solute trapping and a change in solidification morphology from dendritic to cellular accompany the plateau. Based on the results for pure nickel, the second plateau in high undercoolings is hypothesized to be a result of residual oxygen in the alloy system. Further work is needed to quantify the oxygen concentration in alloys and relate the effect of oxygen to solidification velocity at high undercoolings.

The first solidification velocity plateau always occurs for alloys in intermediate undercoolings regardless of k_E. The IMS model does not predict a plateau in solidification velocity for high k_E alloys.
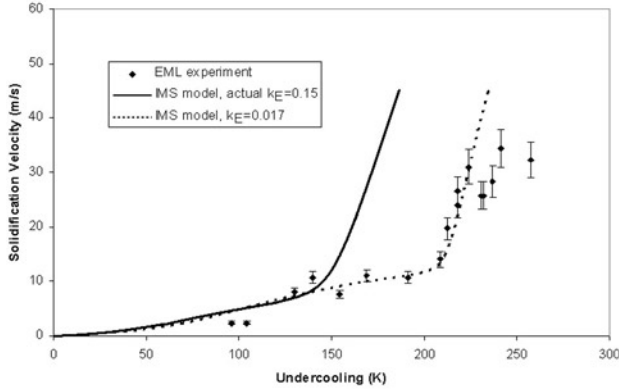
Figure 15: IMS modeling applied to Ni-1.7$^a/_o$C with actual k_E and calculational k_E used for fitting data.
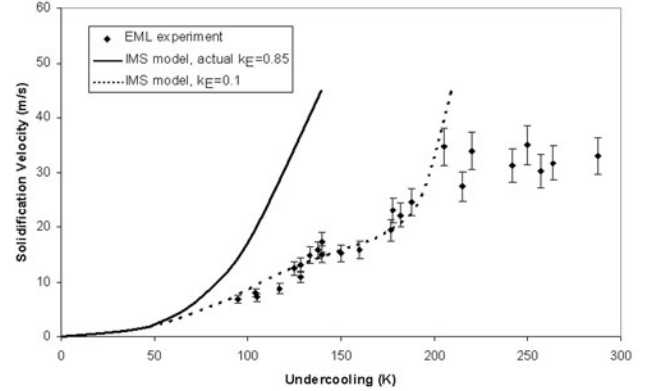

Figure 16: IMS modeling applied to Ni-5$^a/_o$Ti with actual k_E and calculational k_E used for fitting data.

Table 2: Parameters used in applying IMS model to Ni-1.7$^a/_o$C and Ni-5$^a/_o$Ti in figures 15 and 16 respectively.

	Ni-1.7$^a/_o$C, figure 15	Ni-5$^a/_o$Ti, figure 16
T_m (K)	1726	1726
L (J/mol)	17120	17120
C (J/molK)	43	43
a_o (m)	4×10^{-10}	4×10^{-10}
m_L (K/at%)	-14	-6
C_o (at%)	1.7	5
α (m^2/s)	6×10^{-6}	10^{-5}
D (m^2/s)	2.8×10^{-8}	6×10^{-8}
V_o (m/s)	4036	4036
σ (J/m^2)	0.21	0.23

The IMS model conforms to experiment for dilute alloys if the equivocal parameters are adjusted to fit experimental data and a calculational k_E is chosen that is less than the actual k_E of the alloy.

Finally, more theoretical and experimental work is needed in ternary systems and large k_E alloys in order to develop a model that fits experimental results.

[1] W.J. Boettinger, S.R. Coriell and R. Trivedi in: *Rapid Solidification Processing: Principles and Technologies*, eds. R. Mehrabian and P.A. Parrish, Claitor's Publishing, Baton Rouge, LA, 1988, p. 13.
[2] G.P. Ivantsov, Dokl. Akad. Nauk S.S.S.R.,1947, **58**, 567.
[3] J.S. Langer and H. Müller-Krumbhaar, *Acta Metall.*, 1978, **26**, 1681.
[4] M.J. Aziz, *J. Appl. Phys.*, 1982, **53**, 1158.
[5] M.J. Aziz and T. Kaplan, *Acta Metall.*, 1988, **36**, 2335.

[6] J.L. Walker in: *Principles of Solidification*, ed. B. Chalmers, John Wiley & Sons, Inc., New York, NY, 1984, p. 114.

[7] E. Schliep, R. Willnecker, D.M. Herlach and D.P. Gorler, *Proc. 6th Int. Conf. On Rapidly Quenched Metals*, Montreal, Canada, 1987.

[8] G.A. Colligan and B.J. Bayles, *Acta metall.*, 1962, **8**, 895.

[9] B.T. Bassler, W.H. Hofmeister, G. Carro and R.J. Bayuzick, *Metall. Trans.*, 1994, **25A**, 1301.

[10] K. Eckler, D.M. Herlach, R.G. Hamerton and A.L. Greer, *Mater. Sci. Engng*, 1991, **A133**, 730.

[11] R. Willnecker, D.M. Herlach and B. Feuerbacher, *Phys. Rev. Lett.*, 1989, **62**, 2707.

[12] S. Walder and P.L. Ryder, *Mater. Sci. Engng*, 1995, **A203**, 197.

[13] D. Matson, Ph.D. thesis, Massachusetts Institute of Technology, 1996.

[14] B.T. Bassler, Ph.D. thesis, Vanderbilt University, 1997.

[15] R.F. Cochrane, S.E. Battersby and A.M. Mullis, TMS Annual Meeting, San Antonio, TX, 1998.

[16] J. Lipton, W. Kurz and R. Trivedi, *Acta Metall.*, 1987, **35**, 957.

[17] B.T. Bassler, R.S. Brunner and W.H. Hofmeister, *Rev. Sci. Instrm.*, 1997, **68**, 1846.

[18] A.S. Altgilbers, Ph.D. thesis, Vanderbilt University, 2002.